Nanoscale
Horizons

Hyperspectral mapping of anisotropy

Journal:	*Nanoscale Horizons*
Manuscript ID	NH-COM-05-2019-000340.R1
Article Type:	Communication
Date Submitted by the Author:	22-Jul-2019
Complete List of Authors:	Ryu, Meguya; Tokyo Institute of Technology - Ookayama Campus Honda, Reo; Tokyo Institute of Technology - Ookayama Campus Balcytis, Armandas; Swinburne University of Technology, Nanotechnology Vongsvivut, Jitraporn; Australian Synchrotron Co Ltd, Infrared Microspectroscopy Beamline Tobin, Mark ; Australian Synchrotron Co Ltd Juodkazis, Saulius; Swinburne University of Technology, Nanotechnology Morikawa, Junko; Tokyo Institute of Technology - Ookayama Campus

Conceptual insights

We show how the anisotropy of the real and imaginary part of refractive index can be extracted in hyperspectral imaging. Orientation of the absorbing dipoles as well as orientation of the slow (fast) axis can be determined at each pixel in addition to the spectral information. It is shown that refractive index anisotropy - the birefringence - has a contribution in the transmission signal that is usually accounted as absorbance. Discrimination between birefringence and dichroism will improve sensitivity of IR spectroscopy and sensors at molecular fingerprinting spectral range.

Journal Name

ARTICLE TYPE

Cite this: DOI: 10.1039/xxxxxxxxxx

Received Date
Accepted Date

DOI: 10.1039/xxxxxxxxxx

www.rsc.org/journalname

Hyperspectral mapping of anisotropy†

Meguya Ryu,[a] Reo Honda,[a], Armandas Balčytis[b], Jitraporn Vongsvivut[c], Mark J. Tobin[c], Saulius Juodkazis[b,d,e] and Junko Morikawa[a]

Anisotropy of absorbance (dichroism) and birefringence limits spatial resolution, sensitivity dur-ing quantitative detection of trace analytes, as well as spectral imaging at near-IR and mid-IR spectral ranges. Here we show hyperspectral imaging capable of determining retardance and absorbance due to small changes of the real and imaginary parts of refractive index $\sim \Delta n$ and $\sim \Delta\kappa$ at each single point of the measurement at diffraction limited resolution. This single-beam technique allows the retrieval of the phase and amplitude information by virtue of a twice different angular dependence of Δn and $\Delta\kappa$ on the sample orientation angle. It has potential applications in analytical science, multi-dimensional optical memory, and forensic/defense/sensor fields.

Conceptual insights

We show how the anisotropy of the real and imaginary part of refractive index can be extracted in hyperspectral imaging. Orientation of the absorbing dipoles as well as orientation of the slow (fast) axis can be determined at each pixel in addition to the spectral information. It is shown that refractive index anisotropy - the birefringence - has a contribution in the transmission signal which is usually accounted as absorbance. Discrimination between birefingence and dichroism will improve sensitivity of IR spectroscopy and sensors at molecular finger printing spectral range. This method is also applicable to the visual and terahertz spectral ranges.

1 Introduction

Anisotropy, defined by directional dependence of mechanical, electrical, thermal, and optical properties as well as by the size of structural components, manifests itself when characterisation of materials is carried out at an increasingly high resolution[1,2]. For optical performance, real and imaginary parts of the refractive index, $\tilde{n} = n + i\kappa$, together with corresponding anisotropies Δn and $\Delta\kappa$, define the optical response of materials through the absorbance and phase delay (retardance). Depending on the characterisation method[3] used, either based on refraction, scattering or absorption, the anisotropy becomes important for a wide range of modern microscopy techniques[4,5] and sensors; where it leads to a loss of analytical precision unless directly determined.

There is an increasing interest in the engineering of materials down to sub-wavelength and atomic (e.g. graphene) scale with a defined set of n, κ. Applications are expanding into active optical devices such as lasers and perfect absorbers[7,8] or optical elements that use geometrical phase and rely on the orientation anisotropy[9] (a change of orientation of the optical axis in the plane perpendicular to the light propagation).

Ellipsometry can retrieve information of the averaged surface nanoscale properties from the reflectivity ratio of the p- and s-components of the light field $r_p/r_s = \tan\Psi e^{i\Delta}$, where parameters Δ, Ψ are related to the amplitude and phase, respectively. However, the knowledge of the pattern's geometry is a prerequisite for a non ambiguous result when surfaces have complex nanoscale structures/patterns. A true nanoscale characterisation is possible by nano-tip based scanning techniques. Optical properties $(n + i\kappa)$ of nano-films with thickness of only 100 nm can be measured with lateral resolution of tens-of-nm using scanning near-field optical (SNOM) technique[10,11]. In the fast growing field of 2D materials, a NSOM approach has been developed to measure anisotropy of optical properties with nanoscale resolution on atomically thin films bound by van der Waals forces[12–14]. How absorbance and retardance can be measured with high resolution using far-field methods is a continuing quest, which has led to development of a number of super-resolution imaging techniques[15,16]. The focus of this study was on improving the simplest far-field diffraction limited imaging in the IR molecular finger printing spectral range by separation of the retardance and absorbance contributions in transmission.

---

[a] Tokyo Institute of Technology, Meguro-ku, Tokyo 152-8550, Japan
[b] Nanotechnology facility, Swinburne University of Technology, John st., Hawthorn, 3122 Vic, Australia
[c] Infrared Microspectroscopy Beamline, Australian Synchrotron, Clayton, Victoria 3168, Australia
[d] Melbourne Center for Nanofabrication, Australian National Fabrication Facility, Clayton 3168, Melbourne, Australia
[e] Tokyo Tech World Research Hub Initiative (WRHI), School of Materials and Chemical Technology, Tokyo Institute of Technology, 2-12-1 Ookayama, Meguro-ku, Tokyo 152-8550, Japan

† Supplementary Information available.

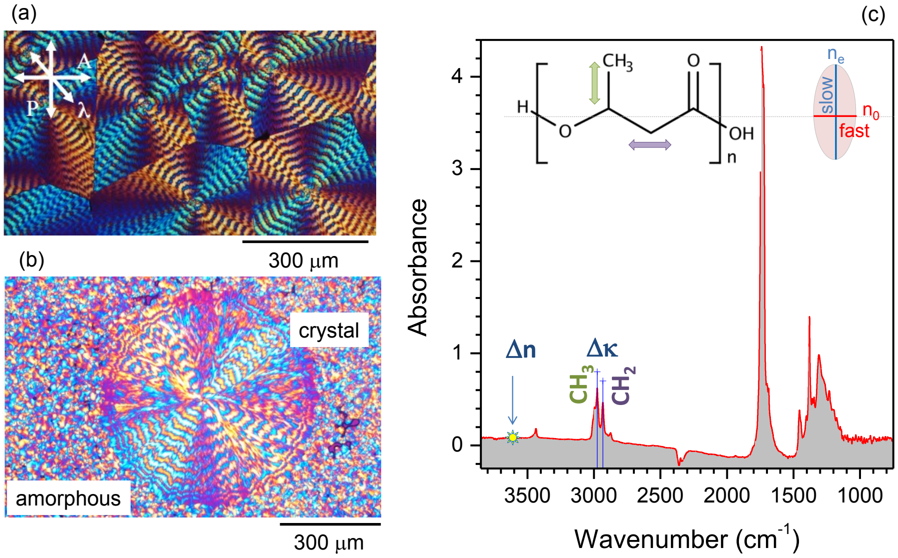

Fig. 1 Poly-hydroxybutyrate (PHB) banded spherulites formed between two CaF_2 substrates. Spherulite radius is 50 - 200 μm with the band pitch of 10 μm and thickness $d \simeq 12$ μm. Polycrystalline film (a) and a single crystalline spherulite grown from the molten amorphous phase (b) shown in color-shifted cross-polarised images; P,A marks transmission of the linear polariser and analyser, respectively. (c) Integrated absorbance spectrum of PHB at $\theta = 90°$; inset shows the chemical structure. The long axis of the refractive index ellipsoid is perpendicular to the molecular chain with $n_e > n_o$ defined by extraordinary and ordinary refractive indices; note, this is particular to PHB crystal while for the most common cases the structural chain alignment corresponds to the slow axis, hence, n_e[6]. Spectral positions of the perpendicular asymmetric stretching modes used for absorption anisotropy, $\Delta\kappa$, detection at CH_3 at 2976 cm^{-1} and CH_2 at 2933 cm^{-1} are marked. The refractive index anisotropy, Δn, was measured at 3600 cm^{-1}.

The absorbance and retardance are both determined from the optical transmittance, T. Birefringence and optical activity, the birefringence of circularly polarised light, is visualised by cross-polarised imaging and defines the retardance $\Delta n \times d/\lambda$ at the chosen wavelength, λ for the sample thickness, d. Retardance can also be determined when polariser and analyser are parallel with a key advantage of a higher light transmission facilitating reliable detection. This becomes very important for chemical imaging in the IR-THz spectral range where absorbance of the sample lowers the transmittance in the cross-polarised measurements of T. The transmittance spectrum, $T(\lambda)$, when reflectance and absorbance are negligible for the parallel polariser and analyser, is given by:

$$T_\theta(\lambda) = 1 - \sin^2 2(\theta-\theta_R)\sin^2(\pi\Delta n d/\lambda), \tag{1}$$

where reflectance, R, and absorbance, A, together with T accounts for the energy balance $R+T+A \equiv 1$, θ is the orientation angle ($\theta = 0$ along the horizontal direction of the view field) and is positive for the anti-clockwise rotation (looking into the beam), θ_R is the slow or fast axis direction; the slow axis is usually aligned to the main molecular chain or along a polymer stretch direction and was used in this study.

The second term on the right-hand side (Eqn. 1) defines T for the crossed polarisers. It is noteworthy that in terms of angular dependence of transmittance, the cross-polarised and parallel alignment of two polarisers are equivalent as they are shifted by $\pi/4$ in respect to each other. When the sample is rotated between two parallel polarisers, the anisotropy of absorpbance can be measured in the same way as with one (the first) polariser, which is the usual way to measure absorbance from transmittance T. This particular feature is important for the method separating absorbance from retardance contributions demonstrated in this study and discussed next.

The orientational anisotropy of absorbance, A_θ, can be determined from the fit of the angular dependence at four arbitrary angles with angular separation of $\pi/4$[17]; more angles were used in this study for a better confidence fit. Absorbance at the orientation angle, θ, at the selected wavelength is given by[17]:

$$A_\theta = \frac{A_{max}-A_{min}}{2}\cos 2(\theta-\theta_A) + \frac{A_{max}+A_{min}}{2}, \tag{2}$$

where θ_A is the orientation azimuth angle of the absorbing dipoles; in general case $\theta_A \neq \theta_R$[18]. This four-angle method was recently applied to determine the anisotropy of absorbance in silk in the mid-IR spectral range[19].

The origin of anisotropy of the real part of refractive index, or birefringence Δn and that of imaginary part expressed via absorption coefficient, $\Delta\alpha \equiv 4\pi\Delta\kappa/\lambda$, are both due to a change of alignment between polarisation of the light field and absorbing dipoles. The absorbance for a polarised light field $\mathbf{E}$ is determined by the dipole transition momentum $\mathbf{M}$ of a particular vibration as $A \propto (\mathbf{E}\cdot\mathbf{M})^2$. Hence, the orientation anisotropy defines both the refractive and absorptive properties. The orientation function used to evaluate ordering of the absorbing dipoles is directly obtained from[6,19]:

$$f_\psi = \frac{D-1}{D+2}\times\frac{2}{3\langle\cos^2\alpha\rangle-1}, \tag{3}$$

where the dichroic ratio $D \equiv A_{max}/A_{min} \equiv A_\parallel/A_\perp$ with $\parallel$ orientation corresponding to the $\alpha = 0°$ angle between the chain axis

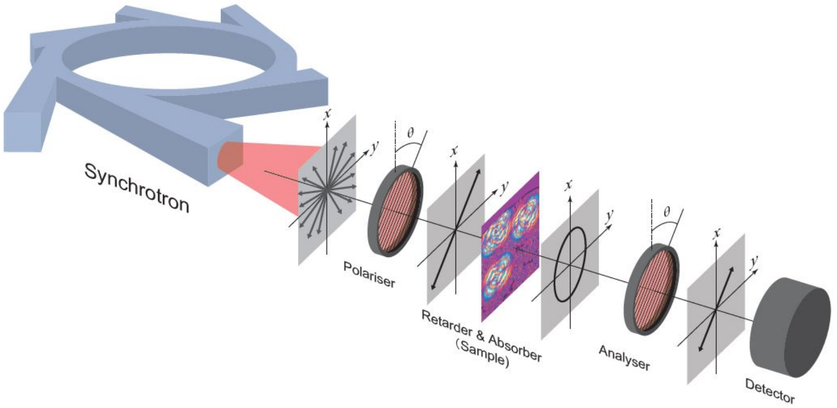

Fig. 2 Setup and principle
dihroism. The angle $\theta = 0^\circ$

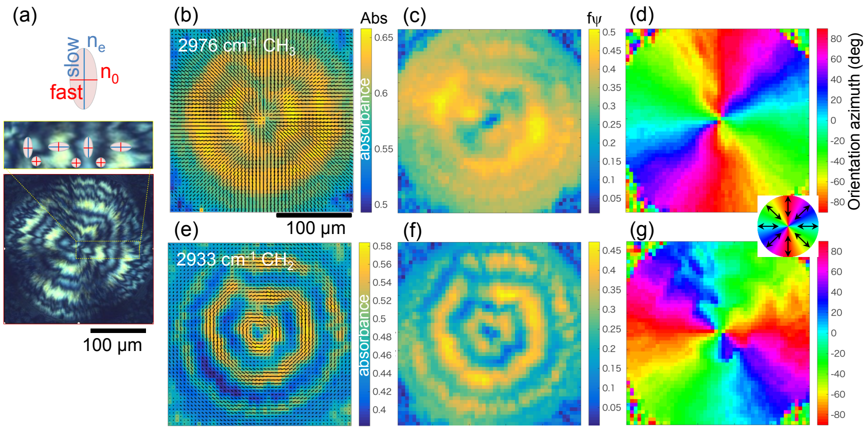

Fig. 3 (a) Optical cross-polarised image of PHB spherulite and schematic presentation of the refractive index ellipsoid; there is no birefringence at the locations of the darkest rings, $n_e = n_o$. (b) Orientation vector map (black lines) calculated from the absorbance fit at $\theta = 0, 30, 45, 60, 90^\circ$ angles overlayed with the average absorbance color map calculated from the 0° and 90° images (min and max absorbance). (c) The orientation function f_ψ [from 0 to 1]. (d) The orientation azimuth map θ_A for the CH$_3$ (inset shows the orientational color map). (e,f,g) Same for CH$_2$ band; note a perpendicular orientation of maps in (g) and (d). Step size in hyperspectral mapping was $5\ \mu$m; lateral resolution $6.9\ \mu$m, and spectral resolution of 4 cm^{-1}. Scale bar of 100 μm for (b-g).

and transition dipole moment, $\langle ... \rangle$ is the ensemble average; the orientation of the CH$_2$ dipole moment (Fig. 1(c)) is defined here as the fast axis. The range of f_ψ values is from 0 to 1, where 1 corresponds to the perfect alignment of the molecular chain axis to the orientation direction, and 0 corresponds to the random case.

By complementing the angular dependence of the hyperspectral mapping of absorbance, $A_\theta(\lambda)$ (Eqn. 2), with that of transmittance $T_\theta(\lambda)$ (Eqn. 1) we show that Δn and $\Delta\kappa$ can be determined in the region of the IR spectrum used for chemical imaging, where usually the absorption is strong.

Here, we introduce an augmented hyperspectral imaging capability to interrogate retardance and absorbance ($\sim \Delta n$ and $\sim \Delta\kappa$) together with the orientation function defined for each single point of measurement down to a diffraction limited resolution. This single-beam technique allows the retrieval of phase and amplitude information by virtue of a twice different angular dependence of Δn and $\Delta\kappa$ on the sample orientation angle. This phase and amplitude sensitive technique has potential applications in analytical science, multi-dimensional optical memory, and classification of optical materials not only by refractive index but also by absorbance symmetries[18].

2 Experimental

2.1 Materials

Samples of poly-hydroxybutyrate (PHB), poly-L-lactic acid (PLLA), paracetamol and silk, which have a different degree of structural complexity, were used for this study (see also the Supplement for the details on other samples). The PHB and PLLA samples were 10-15-μm-thick, while silk was prepared by cryo-microtome and was only $0.1\ \mu$m to test sub-wavelength capability of the hyperspectral imaging in sub-wavelength mode. An optical profilometer was used to measure the height of the PHB and PLLA samples. The difference in height over the IR mapped area was negligible $\pm 2\%$ compared with the average height.

To validate the method, to calibrate and test of the calculation algorithm circular and linear Au grating patterns milled by fo-

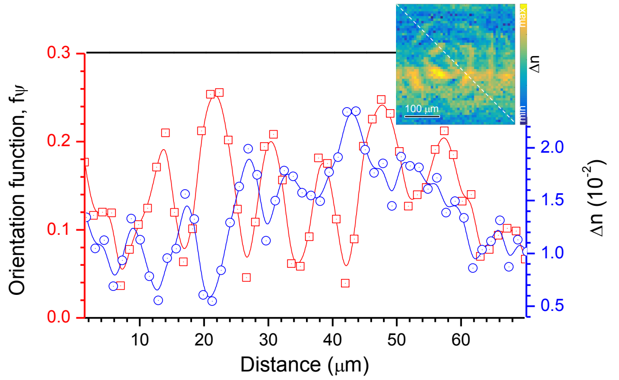

Fig. 4 The diagonal cross sections of the orientation function f_ψ at 2933 cm^{-1} (Fig. 3(f)) and birefringence Δn at 3600 cm^{-1} (inset) maps.

cussed ion beam (FIB; Raith IonLiNE) in a $100-\mu$m-thick Au film sputtered on 30-μm-thick c-cut sapphire were prepared (Supplement Figures II.1 and II.2). A circular grating provides a model of orientational anisotropy and enables the testing of variable anisotropic conditions for single point hyperspectral mapping, i.e. the central regions are more homogeneous in terms of orientation anisotropy per single pixel as compared with the outside regions.

2.2 Polarisation measurements using synchrotron radiation

Hyperspectral imaging of the absorbance and retardance was measured on the IR Microspectroscopy Beamline of the Australian Synchrotron, Melbourne. IR microspectroscopic measurements were performed using a Bruker Hyperion 2000 FT-IR microscope (Bruker Optik GmbH, Ettlingen, Germany) coupled to a Vertex V80v FT-IR spectrometer equipped with a liquid nitrogen-cooled narrow-band mercury cadmium telluride (MCT) detector. Holographic ZnSe wire-grid polarisers (Edmund) were used to set polarisation and for its analysis after the sample (Fig. 2) at the IR spectral range of $\lambda = 4000-750$ cm^{-1} (2.5 - 13.3 μm). The extinction of polarisers was $T^{max}/T^{min} \simeq$150 and overall transmittance ~ 49 and 57% for the two polarisers used for the polariscopy. The far-field transmission measurements were carried out with a numerical aperture $NA = 0.5$, 36× magnification Cassegrain reflecting objective and matching condenser; the corresponding resolution at 3000 cm^{-1} band (λ =3.33 μm) was $0.61\lambda/NA \simeq 4.1$ μm. Mapping of the region of interest (ROI) was carried out by a point-by-point transmittance mapping with step of $2-5$ μm. Typical time required to take an image over typical 50×50 μm^2 area with a 5 μm step was 2-3 hours. Depending on S/N ratio, resolution and ROI area faster scans were optimised to reduce the acquisition time.

Equation 1 based on the Malus law is used for transparent samples and measurements were carried out with polariser-analyser (crossed or parallel). This equation is assuming no absorbance nor its anisotropy, i.e., $\alpha \to 0$, $\Delta\alpha \to 0$. Equation 2 based on Beer-Lambert law is valid for the absorbing samples when transmission, T, is measured with one polariser (no analyser) and does not provide access to the retardance $\sim \Delta n$ (nor n). Both anisotropic effects due to the retardance, $\sim \Delta n$, and absorbance, $\Delta\alpha$, have orientational dependence and cannot be determined with Eqns. 1, 2. Since the anisotropies Δn and $\Delta\alpha$ are inter-related, it is necessary to apply the combined Malus and Beer-Lambert expression (Eqn. 4) for the angular transmission, T_θ. We measured transmittance $T_\theta(\lambda)$ with two parallel polarisers with and without the sample at eight different angles. The data T_θ were fitted with Eqn. 4 to determine the sample's absorbance A_θ and retardance $\sim \Delta n \times d$.

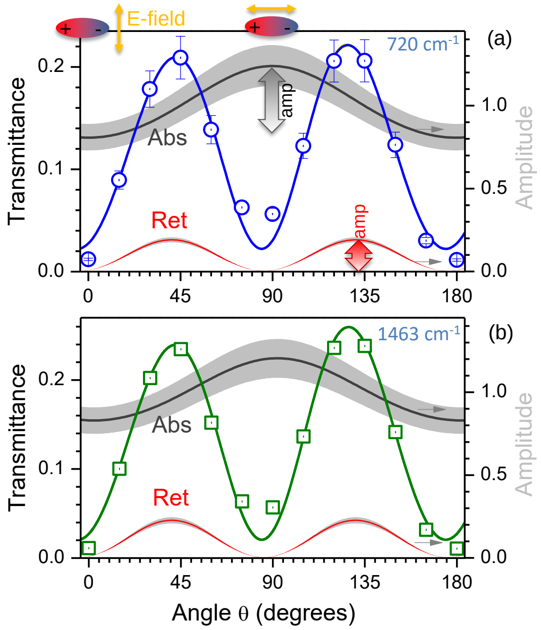

Fig. 5 Experimental (○ and □ dots) and best fit (line) transmission through a cross-polarised setup (second term in Eqn. 1) of polyethy-lene (PE) at two different wavenumbers of CH$_2$ 720 cm^{-1} rocking and 1463 cm^{-1} bending vibrations decoupled into two contributions due to the retardance, Ret, and absorbance, Abs (Eqn. 4); the corresponding amplitudes, amp, are shown on the right axis. The band of $\pm 10\%$ around the best fit Ret and Abs are shown in gray. Equation 4 fit was used with parameters for (a): $a_n = 0.19$, $b_n = 0.69$ rad, $a_\kappa = 0.09$, $b_\kappa = -0.02$ rad, $o = 0.02$ and (b): $a_n = 0.22$, $b_n = 2.26$ rad, $a_\kappa = 0.08$, $b_\kappa = 0.02$ rad, $o = 0.01$. Thickness of the stretched PE film was 12 μm. The top insets show mutual orientations of a dipole and light E-field at 0° ($\perp$) and 90° ($\|$) degrees corresponding to the minimum and maximum absorption, respectively, while the retardance is minimal.

Experimental hyperspectral pixel mapping (x,y) data were imported into a multidimensional matrix with each pixel representing the spectrum λ measured at the orientation θ using Matlab. The proposed method was also tested with a stretched polyethylene film using a single point measurement carried out with a table-top Spectrum One FT-IR spectrometer.

3 Results

Measurements of transmittance performed for each single pixel provide a hyperspectral mapping capability of anisotropy in refractive index, absorbance, and local molecular orientation. Synchrotron radiation was used for material characterisation in the chemical fingerprint spectral region where phase retardance could be measured in the presence of strong absorbance (Fig. 2).

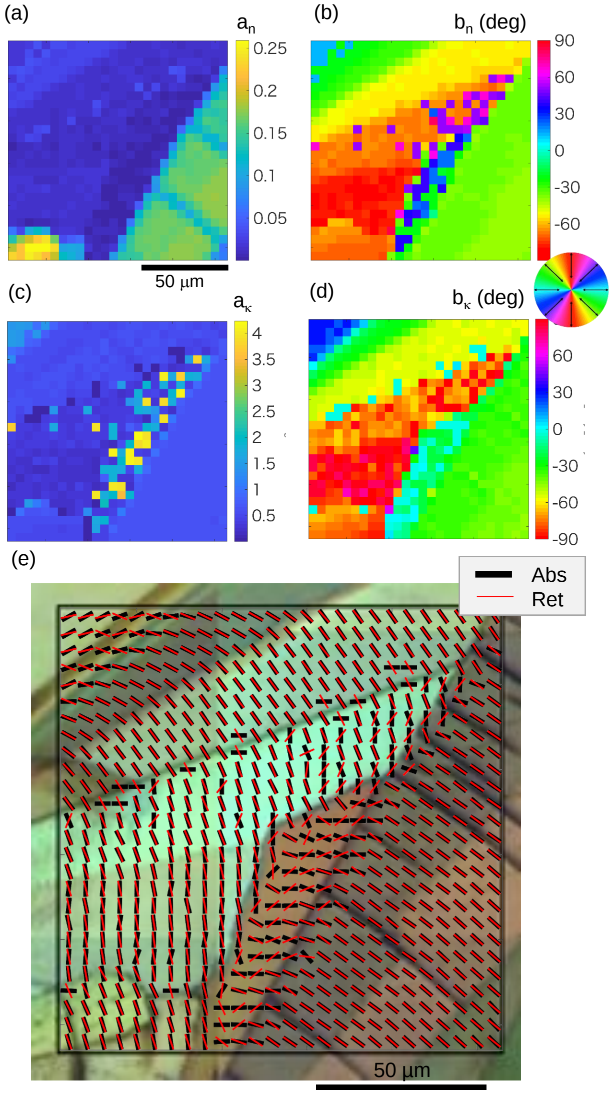

Fig. 6 Hyperspectral mapping of anisotropy in paracetamol (form II) at OH vibration band of 3205 cm^{-1}: the birefringence, Δn, (the retardance *Ret* in Eqn. 4) and dihroism $\sim \Delta\kappa$ (the *Abs* in Eqn. 4) using best fitting to Eqn. 4. The retrieved a_n (a), b_n [deg] (b), a_κ (c), b_κ [deg] (d). (e) Overlayed optical cross polarised image of paracetamol crystal with the orientation vector map of b_n and b_κ. Pixel pitch was 5 μm.

The phase and amplitude sensitive hyperspectral measurement in the IR spectral range of $\lambda = 4000 - 750$ cm^{-1} (2.5 - 13.3 μm) was tested on poly-hydroxybutyrate (PHB) (Fig. 1), poly-L-lactic acid (PLLA), paracetamol, and silk samples which have a different degrees of structural complexity and thicknesses (see, Supplement).

Figure 3 shows absorbance, A, (Eqn. 2) maps at the CH$_3$ and CH$_2$ bands which have perpendicular orientation of the dipole transitions[6,20] (Fig. 1(c)). Local orientation of the absorbing dipoles was calculated using the four polarisation method[17,19] adopted for eight angles for a better fit. The parallel polariser setup was used to measure the transmission, T_θ, and $A_\theta = -\lg(T_\theta)$ were determined using Eqn. 2. The average absorbance $(A_{min} + A_{max})/2$ is plotted as a color map in (b,e) together with the orientation, θ_A, where the length of markers represents the amplitude, *Amp*. Propensity of the molecular orientation, f_ψ, is shown in (c,f) and the orientation of the dipoles, θ_A, in (d,g). This analysis presents an augmented capability of hyperspectral imaging with addition of anisotropy in absorbance and local orientation which are usually not explored in the IR spectral range. In addition, a complimentary capability to map birefringence Δn (Eqn. 1) is demonstrated in Fig. 4. Diagonal cross sections through the spherulite ($\sim 10 - 60$ μm in (c)) show the order distribution at one wavelength and the birefringence at the other; both are anticorrelated. In terms of information recording, the anisotropy in n and κ at different wavelengths can be overlayed in the same pixel of the hyperspectral image.

The anisotropy in both real and imaginary parts of the refractive index can be retrieved by the best fit as is shown next for a single point measurement using a desktop Fourier transform infrared (FT-IR) spectrometer. Transmittance through the parallel polarisers (see, Eqn. 1 assuming $\Delta\kappa = 0$) is affected by the retardance and absorbance of the sample and can be exactly fit by a generic expression of combined Malus and Beer-Lambert laws[21], which accounts for the orientational dependence of transmittance and absorption losses, respectively. It has been established that spectral positions of the measured molecular vibration peaks are affected by the refractive index as well as by the intrinsic absorbance of the molecular vibrations[22]. Absorption peaks are dependent on the method of optical measurement and molecular environment[22] which we observed in IR spectra of silk when measured by different far- and near-field techniques[10,11]. Similar to ellipsometry, we introduce generic expression which combines the Malus and Beer-Lambert laws in the following form:

$$T_\theta = a_n \cos^2 2(\theta - b_n) \times 10^{-a_\kappa \cos^2(\theta - b_\kappa)} + o \equiv Ret \times Abs + o, \quad (4)$$

where the two contributions due to an anisotropic phase delay *Ret* and due to an amplitude change caused by absorbance *Abs* are taken into account at the orientation angle θ; additional sample orientation dependent angles b_n, b_κ [rad] with the offset o were used for the best fit.

Equation 4 reflects the twice different angular dependence of the retardance $\sim \Delta n$ and absorbance $\sim \kappa$ when measured in crossed (or parallel) polariser setup and is the key for separation of the two contributions by the best fit. The double angle 2θ-dependence of Δn reflects the fact that transmittance is minimum when a linearly polarised E-field of light is aligned or is perpendicular to the parallel polariser setup (Eqn. 1), while the absorbance is always defined by E-field projection onto the axis of the dipole transition (hence a θ-dependence).

The principle of additive contributions to transmittance due to phase delay (retardance) and absorbance (losses) is demonstrated for the polyethylene at two different absorption bands of the CH$_2$ vibrations (Fig. 5) measured with a table-top FT-IR spectrometer (SpectrumOne, PerkinEmler). The amplitudes of the two harmonics for Δn and $\Delta\kappa$ are retrieved by the best fit Eqn. 4 regardless of the average values which are proportional to n and κ. A self-referenced character of the measurement provides high fidelity hyperspectral information of anisotropies Δn and $\Delta\kappa$ together with the orientation function per single measured pixel/point. This shows the principle of anisotropy detection and can be carried out in the hyperspectral mapping mode (Figs. 3 and 4). This validates the conjecture expressed by Eqn. 4.

Next, the fitting procedure introduced, validated for a single-point spectral measurement (Eqn. 4), was tested for the hyperspectral mapping of anisotropy using a single transmission measurement, T_θ, with parallel polarisers at selected orientation angles, θ. Paracetamol crystals[23] were chosen due to a well defined domain structure and mapping at the 3205 cm^{-1} OH band[24] responsible for the hydrogen bonding was carried out. Figure 6 shows the retrieved best fit data for the amplitudes, $a_{n,\kappa}$, and orientation angles, $b_{n,\kappa}$. The orientation map for the corresponding retardance, *Ret*, and dihroism, *Abs*, parts of Eqn. 4 were overlaid with an optical cross-polarised image. The domain structure and prevailing orientation are revealed and show the orientational dependence of birefringence and dichroism. Additionally, such hyperspectral imaging shows the retardance in the standard absorbance map (see Supplement for details). The amplitude of the angular dependence T_θ (Eqn. 1) is directly related to the optical retardance, $\Delta nd/\lambda$, via $T^{max} - T^{min} = \sin^2(\pi\Delta nd/\lambda)$. The amplitude of the absorbance in Eqn. 4 is related to the dichroism, Δ'', as:

$$(A_\parallel - A_\perp)/2 = k(\kappa_\parallel - \kappa_\perp)d \equiv \Delta'', \qquad (5)$$

where $k = 2\pi/\lambda$ is the wavevector and the dichroism Δ'' defines losses in the transmitted power, T, at the maximum and minimum orientations $e^{-\Delta''} = \sqrt{T_\parallel/T_\perp}$. This shows the possibility of imaging the absorbance and retardance for any wavelength used for the hyperspectral imaging at a single pixel level.

4 Conclusions and Outlook

In summary, the anisotropy in n and κ together with orientation function f_ψ at different wavelengths can be measured at a single irradiation point as well as by hyperspectral mapping with sub-wavelength resolution in the IR fingerprint spectral range (see, Supplement for additional information). The retardance and absorbance related to the phase and amplitude of the transmitted light can be retrieved using a two parallel polariser setup. We show that two contributions in transmitted signal due to retardance and absorbance are inherently inter-related but can be measured separately by applying combined Malus and Beer-Lambert laws introduced in this study. Separation of contributions due to real and imaginary parts of refractive index become possible due to their different angular dependencies as shown by the proposed expression (Eqn. 4) of the combined law. This expands the application potential of the hyperspectral mapping in multi-dimensional optical memory[25] applications and sensors where high sensitivity measurements are anisotropy dependent.

As is shown here, the phase-related measurement is always affected by the presence of birefringence and anisotropy of absorption. Likewise, the absorbance is affected by the phase retardation. The presented technique of hyperspectral mapping of Δn and $\Delta\kappa$ can be further enhanced by ultra-fast spectral acquisition using the dual-comb spectroscopy[26]. The hyperspectral character of spectral mapping when each pixel has all spectral information is now enriched by measured absorber orientation and its strength with separated contributions due to the real and imaginary parts of the refractive index. This multi-data characterisation of materials at nano-/micro-scales can be further utilised by emerging material characterisation techniques based on the big data approach[27]. Recently, we introduced the four polarisation method at the Australian synchrotron for measurements using focal plane array which dramatically reduced image acquisition time[28] as compared with point-by-point mapping used in this study. One can expect that hyperspectral imaging at near-IR, visible and terahertz spectral ranges using the proposed method will reveal more details about molecular alignment and anisotropy. Also, we envisage applications in aerial and satellite spectral mapping for defence and environmental monitoring.

Acknowledgements

JM acknowledges a partial support by a JSPS KAKENHI Grant No. 18H04506 and JST CREST JPMJCR18I7 grant, Japan. MR acknowledges a partial support by a JSPS KAKENHI Grant No. 18J14350, Japan. We acknowledge partial support via ARC Discovery DP170100131 grant. Experiments were carried out via beamtime project No. 12107 on the IR Microspectroscopy Beamline at the Australian Synchrotron, part of ANSTO. We are grateful to Jingliang Li for the silk sample.

Conflict of interests. None.

Contributions. S.J. and J.M. come up with the idea of experiments, M.R., R.H., A.B., J.M., S.J. carried out experiment at Melbourne synchrotron on the beamline under supervision of J.V. and M.T., M.R. carried our microtome and spectral analysis, R.H. worked on data and image processing. All the authors participated in discussion and analysis of the results and contributed to editing of the manuscript.

Notes and references

1 E. A. Muller, B. Pollard, H. A. Bechtel, P. van Blerkom and M. B. Raschke, *Science Advances*, 2016, **2**, e1601006.
2 J. Chae, S. An, G. Ramer, V. Stavila, G. Holland, Y. Yoon, A. A. Talin, M. Allendorf, V. A. Aksyuk and A. Centrone, *Nano Lett.*, 2017, **17**, 5587 – 5594.
3 E. Bertie and K. H. Michaelian, *J. Chem. Phys.*, 1998, **109**, 6764 – 6771.
4 R. M. Power and J. Huisken, *Nat. Methods*, 2017, **14**, 360–373.
5 M. Padgett, *Opt. Express*, 2017, **25**, 11265–11274.
6 Y. Hikima, J. Morikawa and T. Hashimoto, *Macromolecules*, 2013, **46**, 1582 – 1590.
7 L. Zhang, Z. Bai, H. Ban and L. Liu, *Phys. Chem. Chem. Phys.*, 2015, **17**, 29007.
8 N. I. Landy, S. Sajuyigbe, J. J. Mock, D. R. Smith and W. J. Padilla, *Phys. Rev. Lett.*, 2008, **100**, 207402.
9 M. Khorasaninejad and F. Capasso, *Science*, 2017 (10.1126/science.aam8100).
10 M. Ryu, H. Kobayashi, A. Balcytis, X. Wang, J. Vongsvivut, J. Li, N. Urayama, V. Mizeikis, M. Tobin and S. Juodkazis, *Mater. Res. Express*, 2017, **4**, 115028.
11 M. Ryu, R. Honda, A. Cernescu, A. Vailionis, A. Balcytis, J. Vongsvivut, J.-L. Li, D. Linklater, E. Ivanova, V. Mizeikis, M. Tobin, J. Morikawa and S. Juodkazis, *Beilstein J. Nanotechnol.*, 2019, **10**, 922–929.
12 D. Hu, X. Yang, C. Li, R. Liu, Z. Yao, H. Hu, S. G. Corder, J. Chen, Z. Sun, M. Liu and Q. Dai, *Nature Comm.*, 2017, **8**, 1471.
13 P. Li, I. Dolado, F. Alfaro-Mozaz, F. Casanova, L. Hueso, S. Liu, J. Edgar, A. Nikitin, SVélez and R. Hillenbrand, *Science*, 2018, **359**, 892–896.
14 W. Ma, P. Alonso-González, S. Li, A. Nikitin, J. Yuan, J. Martín-Sánchez, J. Taboada-Gutiérrez, I. Amenabar, P. Li, S. Vélez, C. Tollan,

Z. Dai, Y. Zhang, S. Sriram, K. Kalantar-Zadeh, S.-T. Lee, R. Hillenbrand and Q. Bao, *Nature*, 2018, **562**, 557–562.

15 S. W. Hell and J. Wichmann, *Opt. Lett.*, 1994, **19**, 780–782.

16 P. R. Nicovich, D. M. Owen and K. Gaus, *Nature Protocols*, 2017, **12**, 453–460.

17 Y. Hikima, J. Morikawa and T. Hashimoto, *Macromolecules*, 2011, **44**, 3950 – 3957.

18 M. V. Berry and M. R. Denn, *Proc. R. Soc. Lond. A*, 2003, **459**, 1261–1292.

19 M. Ryu, A. Bačytis, X. Wang, J. Vongsvivut, Y. Hikima, J. Li, M. J. Tobin, S. Juodkazis and J. Morikawa, *Sci. Reports*, 2017, **7**, 7419.

20 C. Merten, T. Kowalik, S. J. Aßhoff and A. Hartwig, *Macromol. Chem. Phys.*, 2010, **211**, 1627 – 1631.

21 M. Born and E. Wolf, *Principles of Optics: Electromagnetic Theory of Propagation, Interference and Diffraction of Light*, 7th edn, 1999.

22 J. E. Bertie and K. H. Michaelian, *J. Chem. Phys.*, 1998, **109**, 6764–6471.

23 M. Haisa, S. Kashino and H.Maeda, *Acta Cryst.*, 1974, **B30**, 2510 – 2512.

24 E. B. Burgina, V. P. Baltakhinov, E. V. Boldyreva and T. P. Shakhtschneider, *J. Struct. Chem.*, 2004, **45**, 64 – 73.

25 P. Zijlstra, J. Chon and M. Gu, *Nature*, 2009, **459**, 410–413.

26 M. Yu, Y. Okawachi, A. G. Griffith, N. Picqué, M. Lipson and A. L. Gaeta, *arXiv*, 2016, arXiv:1610.01121.

27 S. Wu, Y. Kondo, M.-A. Kakimoto, B. Yang, H. Yamada, I. Kuwajima, G. Lambard, K. Hongo, Y. Xu, J. Shiomi, C. Schick, J. Morikawa and R. Yoshida, *NPJ Comput. Mater.*, 2019, **5**, 66.

28 R. Honda, M. Ryu, M. Moritake, V. M. A Balcytis, J. Vongsvivut, M. J. Tobin, D. Appadoo, J.-L. Li, S.-H. Ng, S. Juodkazis and J. Morikawa, *Nanomaterials*, 2019, **9**, 732.